PROCEEDINGS, 49th Workshop on Geothermal Reservoir Engineering
Stanford University, Stanford, California, February 12-14, 2024
SGP-TR-227

Mineralogical Analysis of Silver Peak and Alum Peak Geothermal Well Cores using X-Ray Diffraction (XRD)

Zamakhosi S[1]. Magagula, Zeming Hu[1] , Saeed Salehi[1], Ezat Heydari[2], Amelia Letvin[3], Yuxing Wu[1], John Deymonaz

[1] Hot Lab, 1101 Lexington Ave, Norman, OK 73069, The university of Oklahoma

[2] Dept. of Physics, Atmospheric Sciences, and Geoscience, Jackson State University

[3] Independent Contractor

zeming.hu-1@ou.edu, magagulazamakhosi@gmail.com, salehi@ou.edu, ameliaearheart@gmail.com, ezat.heydari@jsums.edu

Keywords: *XRD, Mineralogy, Core samples, Geothermal wells, Drilling*

ABSTRACT

The success of a geothermal well is dependent on various factors, one of which is the understanding of the subsurface. Knowledge of formation mineralogy allows for an analysis of geothermal capacity and informs efficient drilling fluid design. X-ray diffraction (XRD) provides quantitative bulk analysis that can be combined with core and section analysis to identify sample mineralogy and mineral distribution.

In this study, core samples from two wells in Southwest Nevada, taken at approximately 100 ft intervals with the top interval at 4351 ft and the bottom at 4928 ft, were analyzed in OU's Powder XRD Lab, using Rigaku's Ultima IV Diffractometer and MDI's Jade software. The aim was to identify what the formation mineralogy as well as how this correlated from well to well. When mineral data from the two wells was put side-by-side, there were five mappable zones and a potential faulting or post-erosional deposition system at 4500 ft.

1. Introduction

In the intricate process of designing a drilling program, the consideration of various factors is paramount, with formation mineralogy emerging as a pivotal element. A profound understanding of the mineral composition not only informs meticulous drilling plans but also mitigates the inherent risks associated with formation damage or issues such as clay swelling due to the dynamic interplay between drilling fluid and the formation matrix. In addition, understanding mineralogy in our target zone is also beneficial for the determination of the drilling rate (Khankishiyev & Salehi, 2023; Tumac et al 2023).

Late-phase geothermal exploration involves deep well drilling to validate temperature and permeability. Borehole size, depth, and drilling methods balance cost and information. Continuous core drilling provides detailed data on reservoir fractures and hydrothermal alteration. While more expensive, it enhances understanding. Infrared spectroscopy aids in identifying alteration at depth (Clavin and Pace 2016). Analyzing minerals in near real-time from cuttings at a geothermal drill hole enhances descriptions by well site geologists, aiding in lithotyping and reducing risk and costs (Hu et al., 2023; Vivas et al., 2023). This allows for the recognition and correlation of mineral zones, providing insights into subsurface temperature distributions, resource assessment, and locating recharge and discharge zones (Hamilton et al 2016; Khankishiyev et al. 2023).

Within the industry, X-Ray Diffraction (XRD), thin section petrography, scanning electron microscope/energy dispersive X-ray spectrometry (SEM/EDS), or Fourier Transform Infrared (FTIR) spectrometry are utilized for robust mineral identification. These methods leverage electromagnetic radiation to yield bulk mineralogy results. Yet XRD and FTIR diverge in their interaction with the material under scrutiny. FTIR discerns the chemical composition based on covalent bond frequencies, while XRD delves into the physical structure by gauging lattice spacing (Ruessink and Harville 1992). Although both methods provide comparably accurate results, each harbors distinct advantages. FTIR excels in analyzing poorly ordered minerals, whereas XRD proves superior in the meticulous scrutiny of clay minerals and halides. This investigation opts for XRD, a deliberate choice aimed at enhancing the precision of clay and halide analysis. The investigation's goal was to analyze formation mineralogy to factor it into the decision to further develop plan for geothermal use in drilling field.

2. METHODOLOGY

To obtain mappable results from the two wells, samples were taken at about 100 ft intervals for both wells between 4350 and 4928 ft. Each sample was crushed, grinded, and then micronized before being mounted in the diffractometer. Sample micronizing is vital to obtaining an accurate XRD spectrum because the larger the particle size the greater the error in peak intensity and width measurements (Speakman, 2022).

2.1 Data Collection

The samples under investigation were cored from two wells located in Esmeralda County in southwest Nevada, shown in Figure 1. Well A was drilled in the Silver Peak field with a planned TVD of 7000ft whereas Well B was drilled in the Alum Peak site with a TVD of 5000 ft. Well A was cored from 4366 to 5409 ft whereas Well B was cored from 4331 to 4867 ft (core images in **Appendix A**).

Figure 1: Esmeralda County, Nevada

2.2 Data Pre-Processing and Cleaning

Prior to loading samples into the diffractometer, micronization was essential. Manual crushing with a hammer was followed by measuring approximately 1 gram of the crushed sample, which was then ground using a grinder assembly. The ground samples were introduced into a micronizing mill, with 7 ml of methanol added to facilitate the process. After a 5-minute micronizing cycle, samples were dried at 50°C to eliminate methanol. Carefully maintaining the sample's random mineral orientation, the dried sample was loaded onto an XRD plate, avoiding excessive pressure, as depicted in **Figure 2.**

Figure 2: The workflow of sample preparation

2.2 Data Pre-Processing and Cleaning

The University of Oklahoma's Powder XRD Lab uses MDI's Jade software which uses Reference Intensity Ratio (RIR) to scale diffraction data to a reference material (corundum), thus keeping all factors except the analyte concentration ratioed and constant. Therefore, the area under each intensity peak is constant and can be used to reverse calculate mineral concentration (ICDD 2022). The XRD plate was carefully placed into the diffractometer, as illustrated in **Figure 3**, with the operational parameters configured. In adherence to the OU standard condition for random mounts (Condition 2), our samples underwent analysis. This condition prescribes 2θ angles ranging from 2 to 70°, a step size of 0.02°, and employs radiation at 76kV and 44 mA. Each scan, lasting approximately 2.5 hours, produces a diffraction spectrum depicting intensity in Angstrom versus 2θ in degrees.

Figure 3: Rigaku Ultima IV X-Ray Diffractometer, a) Exterior view and b) Interior view showing X-ray source and receiver and plate mount.

3 ANALYSIS/EVALUATION & RESULTS

Upon completion of the scan, the raw diffraction spectrum file was imported into MDI's Jade software, utilizing the Whole Pattern Fitting (WPF) approach to identify mineral combinations that closely matched the sample. Each mineral selection was based on the proximity of its intensity value to the corresponding amplitude peak on the spectrum, supplemented by general core analysis knowledge. The software subsequently generated a comprehensive pattern that best matched the chosen mineral peaks. The resulting WPF analysis provided estimates of the mineral composition by weight percentage along with standard deviation value.

In total 13 samples were analyzed: 7 for Well A and 6 for Well B, at approximately 100 ft intervals. In APPDEIX Figures 1 – 6 and Figures 7 – 13 show the diffraction spectra for Well A and B from shallowest to deepest and Figures 4, 5 and 6 summarize the composition at each depth as obtained from WPF analysis.

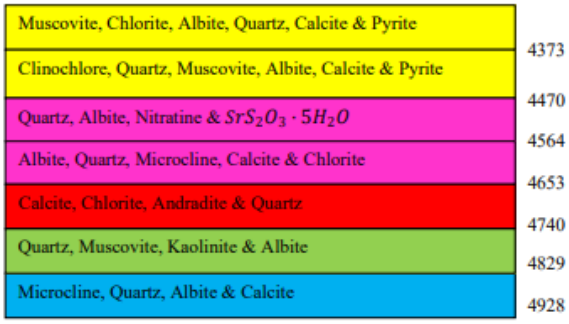

Figure 4: Well A Mineral composition by depth, from most to least abundant per depth

Figure 4 shows the transition of mineralogy from a chlorite-rich zone to a quartzitic and feldspathic zone, then a calcitic zone, then lastly another quartz and feldspar rich zone. In addition, there is a pyrite intrusion at 4373 ft and a strontium thiosulfate pentahydrate presence at 4470 ft.

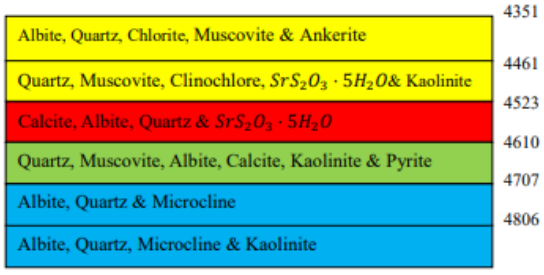

Figure 5: Well B Mineral Composition by Depth from most to least abundant per depth

Figure 5 shows the transition of mineralogy from a quartzitic and feldspathic zone to a calcitic zone, then lastly a feldspar rich zone. It also shows a strontium thiosulfate pentahydrate intrusion between 4461 – 4610ft and a pyrite intrusion between 4610 – 4707ft.

Initial core studies on Well B identified the rock as generally phyllitic so an abundance of muscovite, quartz, and feldspar was expected on the XRD data, and the results in **Figure 6** support this. At depths between 4320 – 4598, core descriptions showed slight phyllite in limestones with interbedded siltstones and casual calcite filled fractures. When compared to the data in **Figure 6**, this matches as the sample are abundant in muscovite, quartz, and feldspar minerals with a calcite rich zone at 4523ft which likely corresponds to a filled fracture. Between 4598 – 4868.5 ft core descriptions described the core as felsic with sericite alterations, pyrite, and quartz monzonite. Sericite alterations are rich in mica and quartz monzonite is rich in quartz and feldspathic minerals, these minerals are abundant where the mica in abundance is muscovite, and albite and microcline are the dominant feldspars. In addition, core description predicted the presence of pyrite in quantities less than 1.5% at 4614 – 4621 ft, and the sample at 4610 ft showed a 1.3% pyrite concentration. This agreement in XRD data instills confidence in the mineralogical analysis conducted.

Thin Section Analysis was conducted on 4 samples from the top 150ft of this well at 4331, 4363, 4463, and 4476.5 ft, showing in the **Appendix C7-13**. Figure 6 below shows the summary of dominant minerals identified.

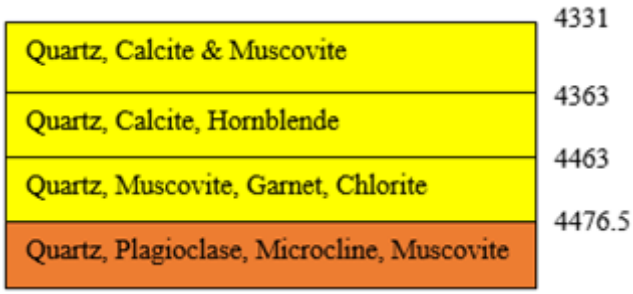

Figure 6: Well B TSA Mineral Composition by Depth from most to least abundant per depth

Figure 6 shows that the dominant mineral in this section is quartz, with a transition from a calcitic zone to a felsic zone. Further image analysis identified the mineralogy of the sample as transitioning from a marble to quartzitic. At each depth, the mineralogy can be described as,

- 4331 – Quartz matrix with calcite intrusions
- 4363 – Quartz and Calcite-rich matrix with Amphibole (Hornblende) intrusions
- 4463 – Muscovite-rich zone with a notable garnet intrusion
- 4476.5 – Quartz & Feldspar-rich matrix with Muscovite filled cracks/fractures

This data is consistent with both XRD and core analysis results with dominant minerals identified in XRD being visibly identifiable on thin sections. The core description from 4320 to 4598 ft identified phyllite in limestone with interbedded siltstones and calcite filled fractures, this description matches the mineralogy description with 4331, 4363, and 4476.5 ft showing a phyllitic zone and 4463 ft showing a possible siltstone zone.

3.1 Comparison between two wells

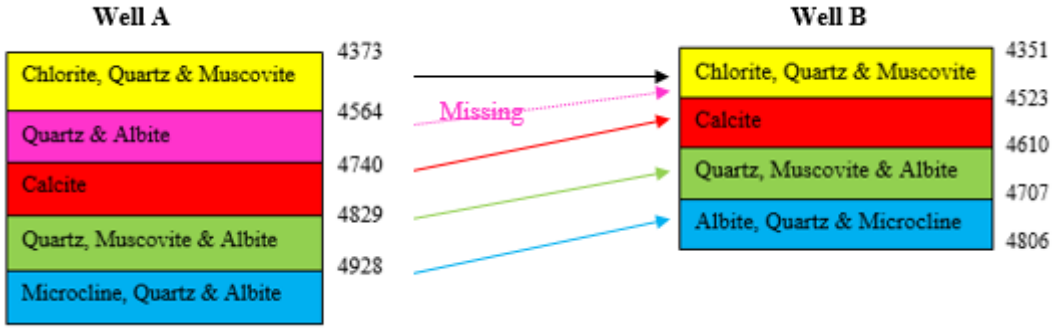

Figure 7: Comparison of Well A and Well B abundant mineral composition by depth from most to least abundant per depth, specific depths are in parentheses for each well in ft

There are 5 apparent zones in the two wells, and these are shown as yellow, purple, red, green, and blue in Figure 19. The yellow zone is around 4351 – 4564 ft and is rich in muscovite, quartz, and chlorite. The purple zone seems to be missing in Well B, it shows a quartz and albite rich zone around 4564 – 4740 ft in Well A. Below 4500ft the 2 wells show different mineralogy, however upon closer inspection at 4740 ft the mineralogy of Well A matches 4523ft on Well B and the depths thereafter have a consistent 200 ft offset. The

red zone is a calcite rich area in both wells which overlies the green zone that is a quartz and muscovite rich area. Lastly the blue zone at the deepest core investigated is a microcline, quartz, and albite rich area.

4. CONCLUSION

Consistency is evident between previous core studies, thin section analysis, and XRD analysis, confirming Well B's phyllitic nature. This supports the hypothesis of calcite-filled fractures and indicates a deeper lithology of quartz monzonite due to its richness in feldspathic minerals. Notably, mineral zones exhibit correlation between Well A and Well B. The offset below 4500 ft suggests potential faulting post-deposition of the quartz and albite layer, placing Well B on the higher block and Well A on the downthrown block. The absence of the quartz and albite zone in Well B implies either post-depositional erosion or intrusion into Well A.

5. REFERENCES

Cement. 2013. Sample Preparation for Quantitative X-Ray Diffraction (XRD/Rietveld), https://www.cementscience.com/2013/01/sample-preparation-for-quantitative-x-ray-diffraction-xrdrietveld.html (accessed November 2023).

Calvin, W.M. and Pace, E.L., 2016. Mapping alteration in geothermal drill core using a field portable spectroradiometer. Geothermics, 61, pp.12-23.

Vivas, C., Hu, Z., and Salehi, S. 2023. Texture-Dependent Thermal Properties of Sandstone Rocks Examined by Scanning Electron Microscopy for Thermal Energy Storage Applications. ASME Open Journal of Engineering, 2.

Hamilton, P.J., Harris, C. and Hillier, S., 2016. Characterization of geothermal systems through FTIR mineral analysis of drill cuttings for exploration, appraisal and development. In Proceedings The 4th Indonesia International Geothermal Convention & Exhibition. Petroleum Field. Proc. 5th Geol. Conf. & Exhibition, Geol. Soc. Trinidad & Tobago.

Hu, Z., Vivas, C., and Salehi, S. 2023. Computer Vision in Predicting Thermal Diffusivity of Subsurface Rocks. Geothermal Resources Council Transactions 47, 2299–2308.

Khankishiyev, O., Salehi, S., Vivas, C., Nygaard, R., & Rehg, D. (2023). Techno-Economic Investigation of Geothermal Development in Sedimentary Basins. ASME Open Journal of Engineering, https://doi.org/10.1115/1.4062412

Khankishiyev, O., & Salehi, S. (2023). Technology Review and Techno-Economic Analysis of Super-Hot EGS Development in Hard Rock Formations. Geothermal Resources Council Transactions, 47, 2979-2997.

ICDD. 2022. About MDI. International Centre for Diffraction Data, https://www.icdd.com/mdi-jade/ (accessed 20 November 2022).

Ruessink, B. H. and Harville, D. G. 1992. Quantitative Analysis of Bulk Mineralogy: The Applicability and Performance of XRD and FTIR Paper presented at the SPE Formation Damage Control Symposium, Lafayette, Louisiana, February 26 1992.

Speakman, Scott. 2022. The challenge of grain size X-Ray powder diffraction analysis of parts made by metal am, https://www.metal-am.com/articles/the-challenge-of-grain-size-x-ray-powder-diffraction-analysis-of-parts-made-by-metal-am/ (accessed November 2023).

Tumac, D., Shaterpour-Mamaghani, A., Hojjati, S., Polat, C., Er, S., Copur, H. and Balci, C., 2023. Determination of drilling rate index based on mineralogical and textural properties of natural stones. Bulletin of Engineering Geology and the Environment, 82(7), p.263.

6. ACKNOWLEDGEMENTS

The authors would like to thank DeepPower and Baseload Power for their support and provision of cores, and for the permission to prepare and present this paper.

7. NOMENCLATURE

Acronyms:

ft	Feet, L
RIR	Reference Intensity Ratio
TSA	Thin Section Analysis
WPF	Whole Pattern Fitting
XRD	X-Ray Diffraction

Symbols:

E	Precision
R	Accuracy

8. APPENDICES

8.1 Appendix A - Core Pictures

Figure A1: Core Images for Well A for 4373, 4470, and 4564 feet from left to right

Figure A2: Core Images for Well A for 4653, 4740, and 4829 feet from left to right

Figure A3: Core Image for Well A for 4928 feet

Figure A4: Core Images for Well B for 4351, 4461, and 4523 feet from left to right

Figure A5: Core Images for Well B for 4610, 4707, and 4806 feet from left to right

8.2 Appendix B – Thin Section Analysis Images

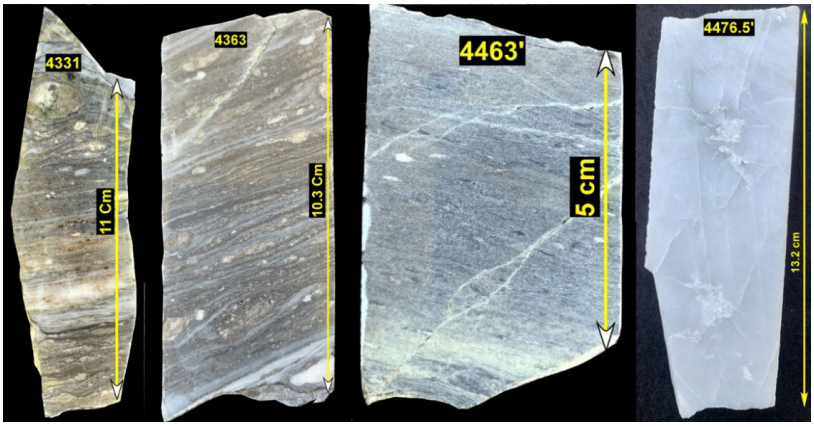

Figure B1: Core Images for Well B at 4331, 4363, 4463, and 4476.5 feet from left to right

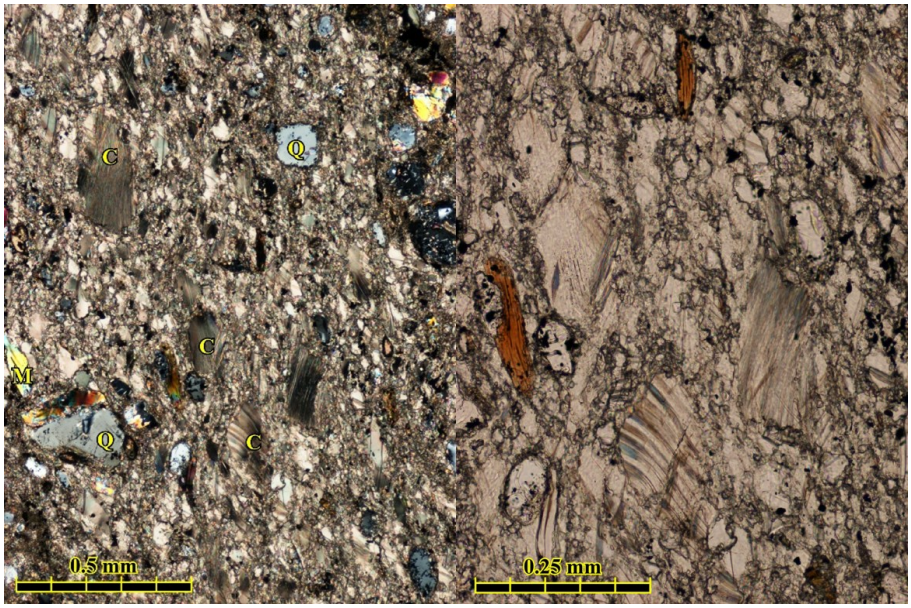

Figure B2: Photomicrographs at 4331 ft at 0.5mm and 0.25mm

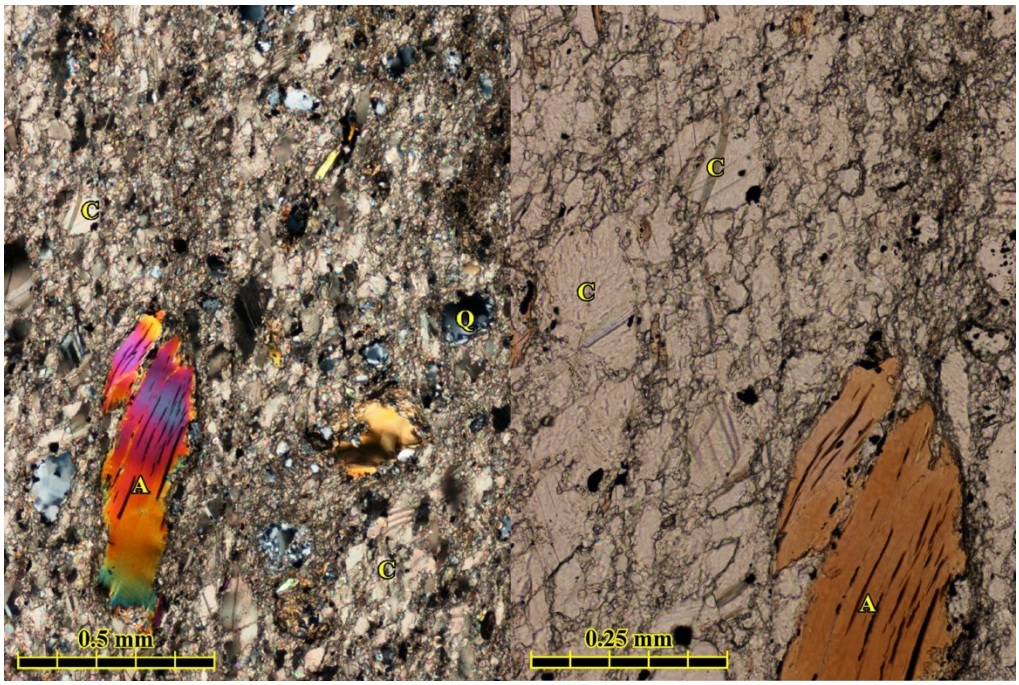

Figure B3: Photomicrographs at 4363 ft at 0.5mm and 0.25mm

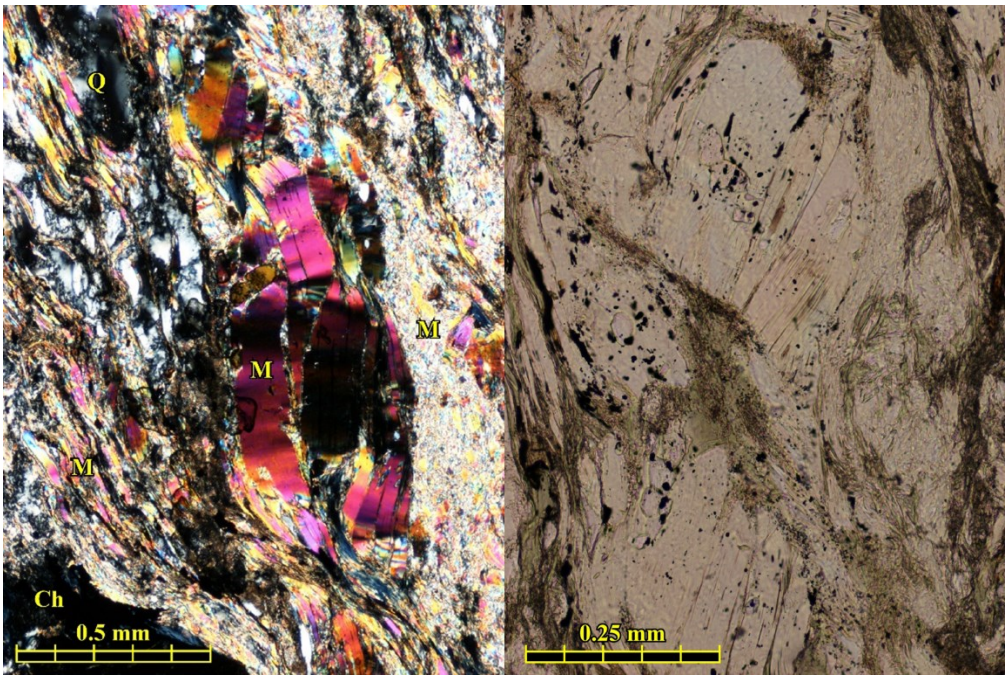

Figure B4: Photomicrographs at 4463 ft at 0.5mm and 0.25mm

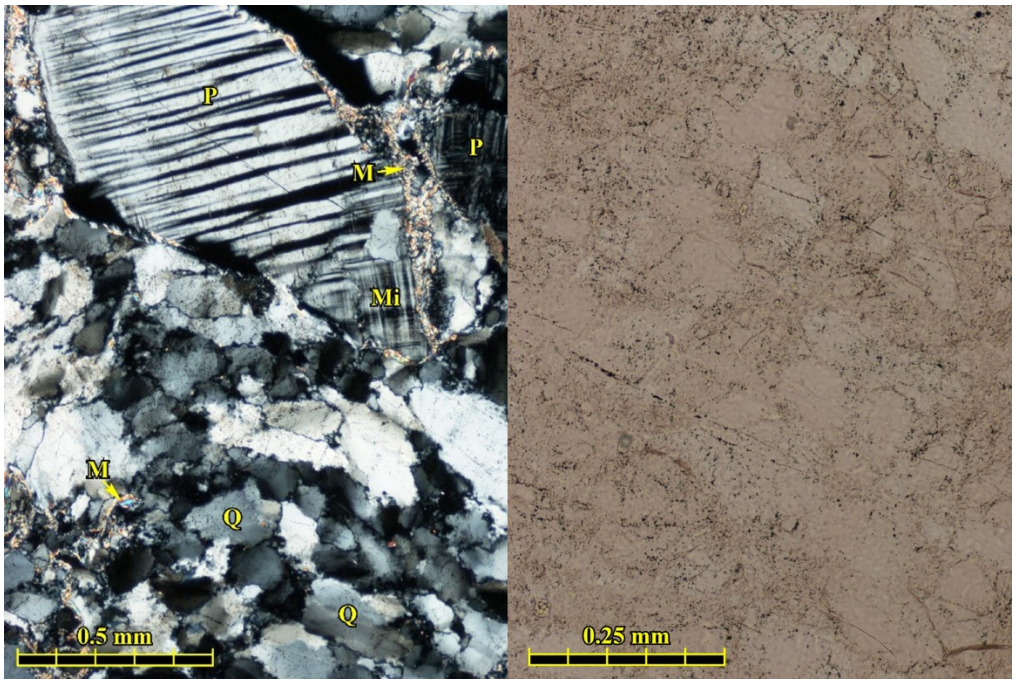

Figure B5: Photomicrographs at 4476.5 ft at 0.5mm and 0.25mm

8.3 Appendix C – Further XRD Results

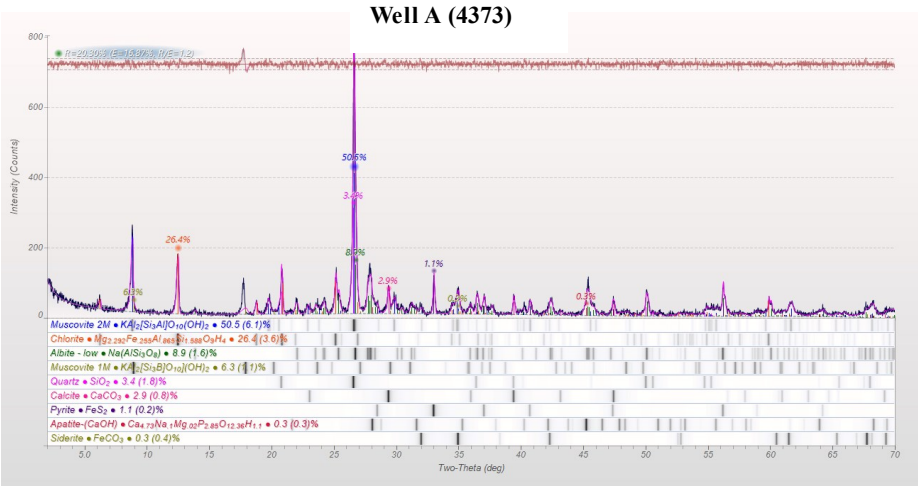

Figure C1: Diffraction spectrum for Well A at 4373 feet with WPF fitted to identified mineral peaks

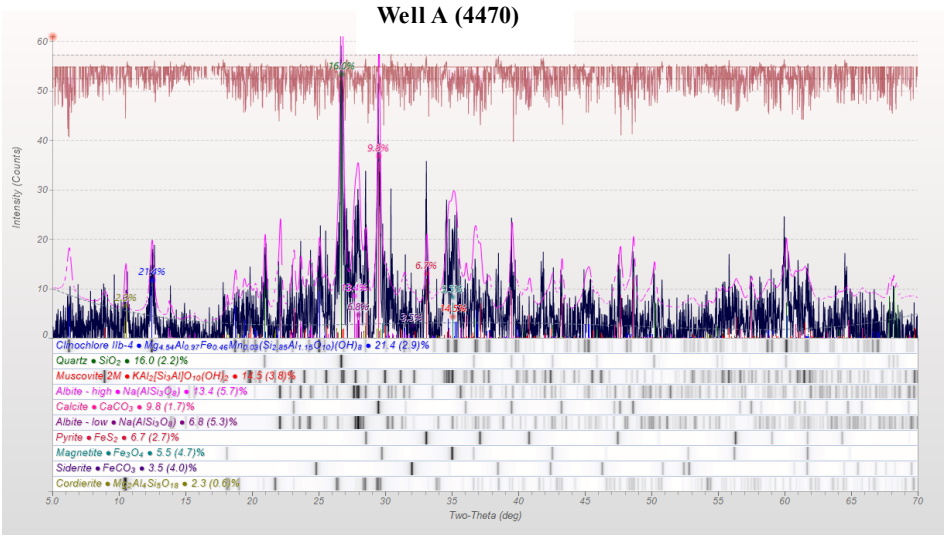

Figure C2: Diffraction spectrum for Well A at 4470 feet with WPF fitted to identified mineral peaks

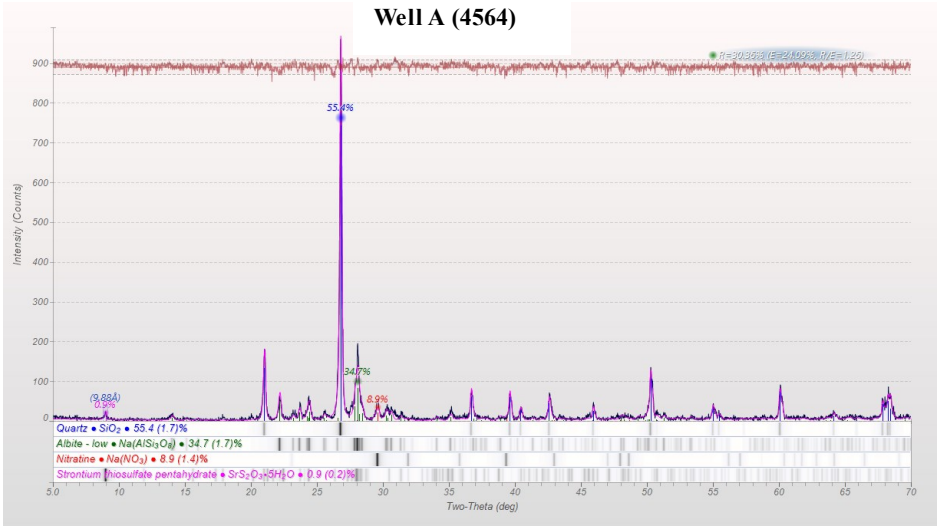

Figure C3: Diffraction spectrum for Well A at 4564 feet with WPF fitted to identified mineral peaks

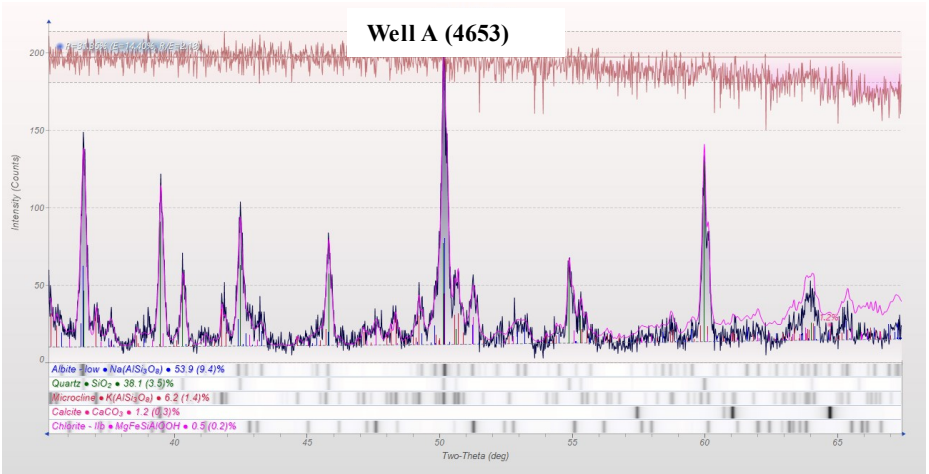

Figure C5: Diffraction spectrum for Well A at 4653 feet with WPF fitted to identified mineral peaks

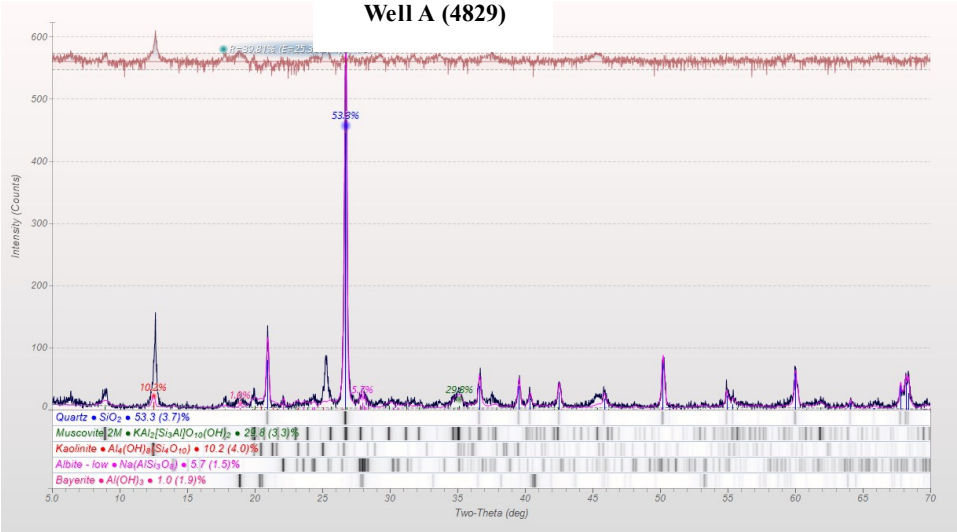

Figure C6: Diffraction spectrum for Well A at 4829 feet with WPF fitted to identified mineral peaks

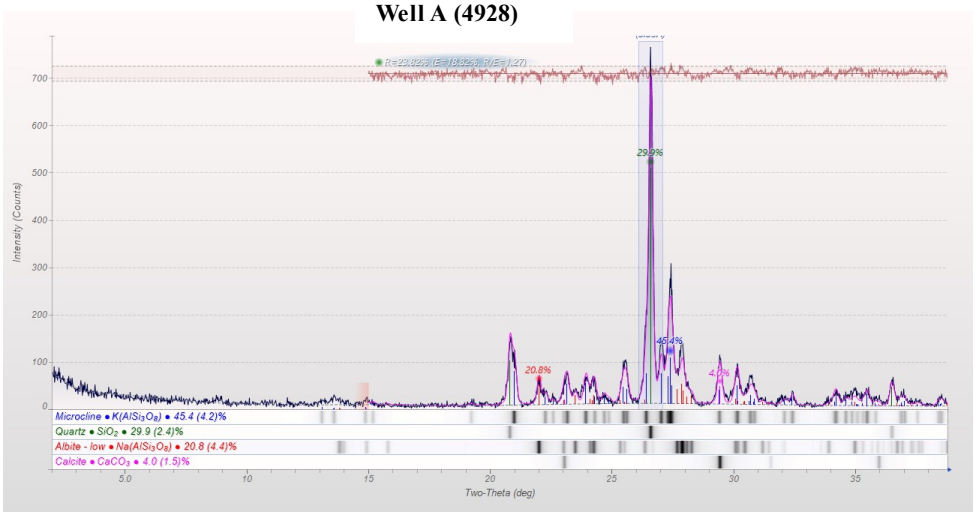

Figure C7: Diffraction spectrum for Well A at 4928 feet with WPF fitted to identified mineral peaks

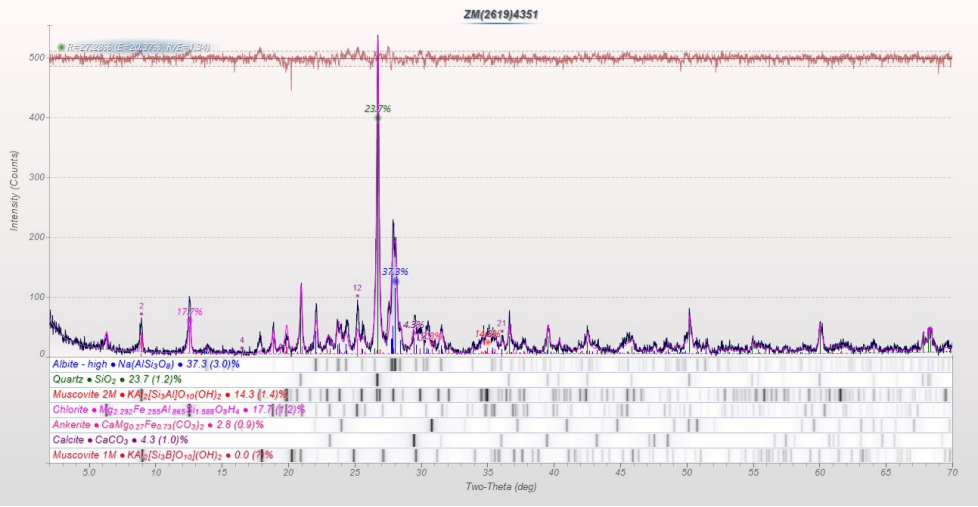

Figure C8: Diffraction spectrum for Well B at 4351 feet with WPF fitted to identified mineral peaks

Well B (4461)

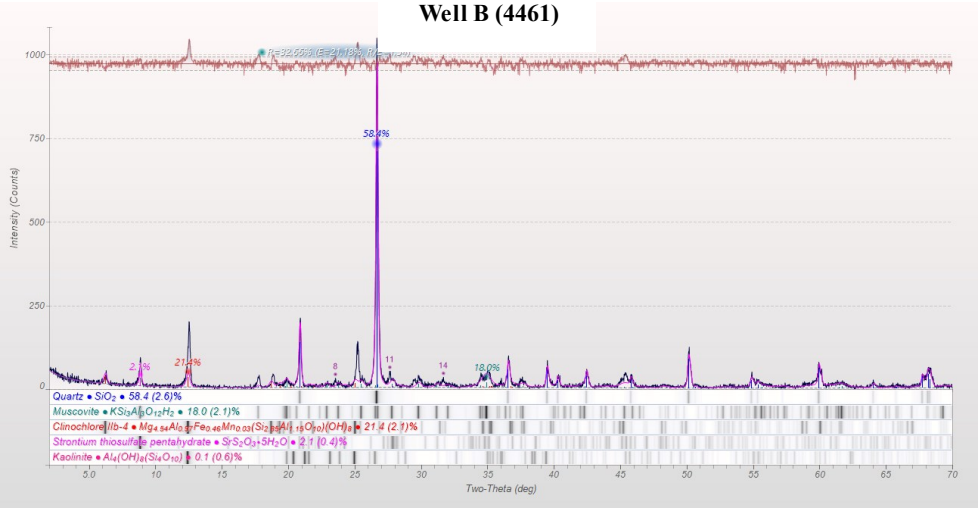

Figure C9: Diffraction spectrum for Well B at 4461 feet with WPF fitted to identified mineral peaks

Well B (4523)

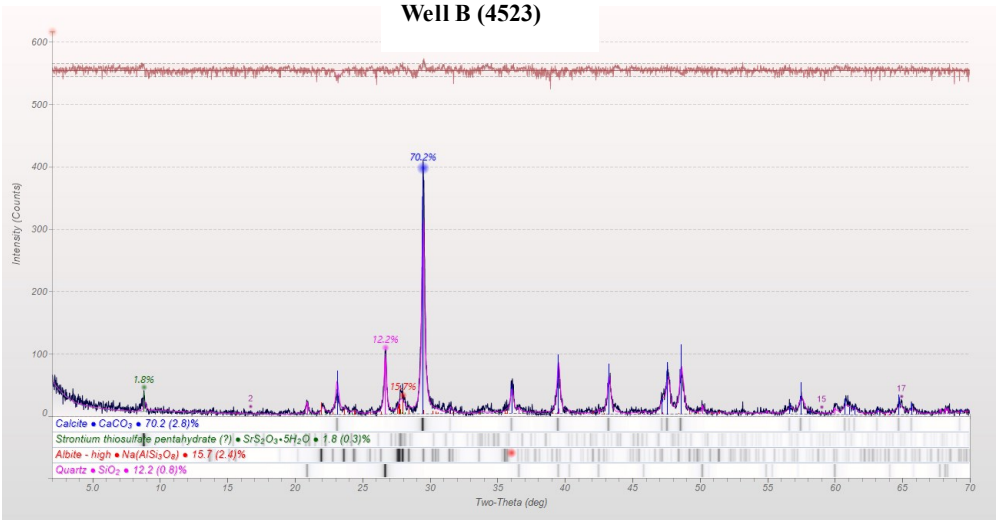

Figure C10: Diffraction spectrum for Well B at 4523 feet with WPF fitted to identified mineral peaks

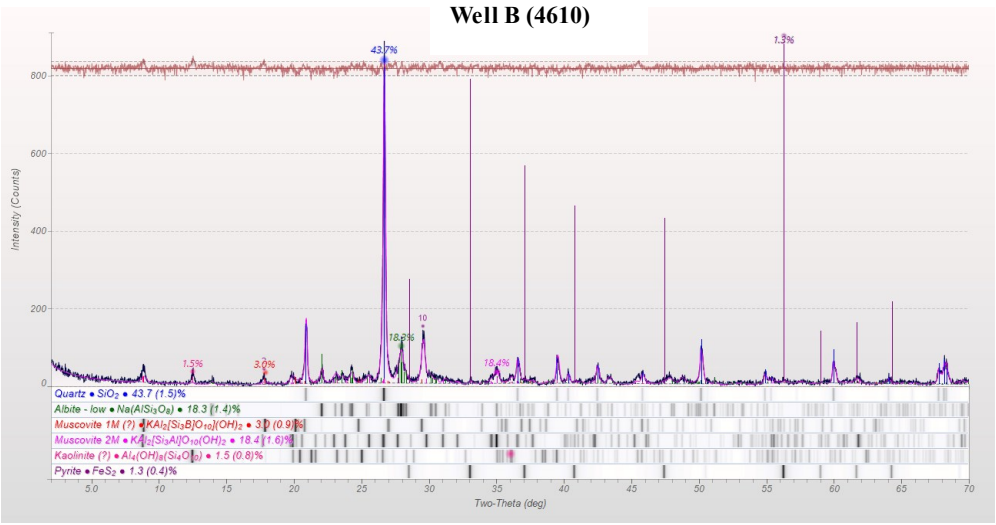

Figure C11: Diffraction spectrum for Well B at 4610 feet with WPF fitted to identified mineral peaks

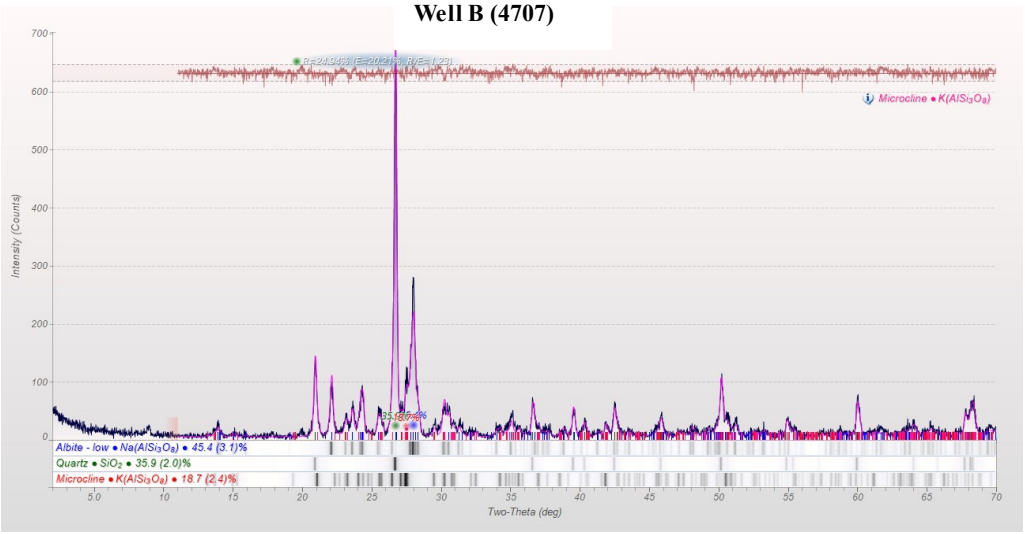

Figure C12: Diffraction spectrum for Well B at 4707 feet with WPF fitted to identified mineral peaks

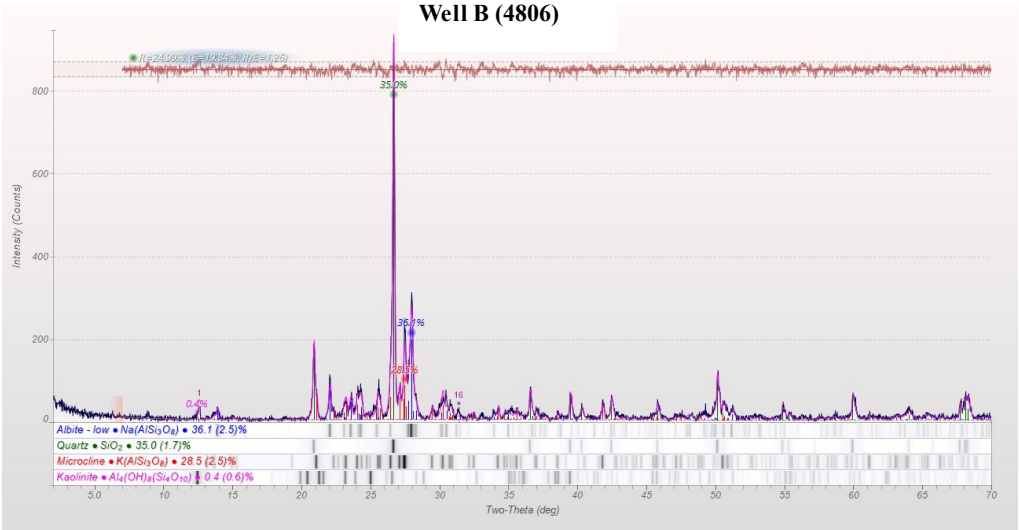

Figure C13: Diffraction spectrum for Well B at 4806 feet with WPF fitted to identified mineral peaks

8.4 Appendix D – Equipment

Figure D1: Micronizing Mill (Source – Cement, 2023)